DOE/ET-53088-108 IFSR #108

THE EFFECTS OF COMPRESSIBILITY ON THE RESISTIVE BALLOONING MODE

T. C. Hender, B. A. Carreras and W. A. Cooper
Oak Ridge National Laboratory

J. A. Holmes
Union Carbide Corporation

P. H. Diamond and P. L. Similon
University of Texas at Austin

September 1983

THE EFFECTS OF COMPRESSIBILITY ON THE RESISTIVE BALLOONING MODE

T. C. Hender, B. A. Carreras, and W. A. Cooper
Oak Ridge National Laboratory, Oak Ridge, Tennessee 37830

J. A. Holmes
Computer Sciences, Union Carbide Corporation Nuclear Division, Oak Ridge, Tennessee 37830

P. H. Diamond, and P. L. Similon
University of Texas at Austin, Institute for Fusion Studies, Austin, Texas 78712

The linear stability of the resistive ballooning mode, as described by the resistive MHD model, is investigated both analytically and numerically. When the pressure evolution is approximated by fluid convection (reduced MHD model), an instability driven by geodesic curvature, with a growth rate $\gamma \sim \eta^{1/3}\beta_p^{2/3}$, is found. For conditions relevant to the Impurity Study Experiment (ISX-B), it is shown that for modest poloidal beta ($\beta_p \simeq 1$), high current, and relatively high temperatures, compressibility has a significant stabilizing influence, relative to the pressure convection model, for low toroidal mode number modes. However, at high β_p ($\gtrsim 2$), low current, and lower temperatures, compressibility has much less effect.

I. INTRODUCTION

Studies of resistive ballooning modes have been made by various authors.[1-5] A possible link between resistive ballooning mode activity and energy transport in high beta tokamaks has been proposed.[6] This transport model has been shown to be in good agreement with experimental results for the Impurity Study Experiment (ISX-B) tokamak.[7] For this transport model and the related study of the nonlinear resistive ballooning mode, the equations used were the reduced high beta tokamak equations, where pressure evolution is approximated by fluid convection, and propagation by coupling to sound waves is neglected. These assumptions result in a resistive ballooning instability driven by geodesic curvature. These modes are extended along the magnetic field lines and have a growth rate given by

$$\gamma = \left(\frac{\beta_0}{\epsilon}\frac{q^2}{\rho}\frac{dP_0}{d\rho}\right)^{2/3}\left(\frac{\eta n^2}{2S}\right)^{1/3} .$$

In this paper the linear stability of the resistive ballooning mode is studied using the full resistive MHD equations. In particular, the effects of pressure evolution by coupling to ion sound waves propagating along and compressing across the magnetic field are retained. Here, the study will focus on the parameter regime relevant to the ISX-B tokamak. Figure 1 indicates the regime we are exploring by plotting the electron temperature at half-radius and β_T, the average toroidal beta, as a function of the safety factor q at the plasma edge. Two plasma current scans at injection powers of 0.91 MW and 2 MW are shown. Ideal MHD stability studies[8] using equilibria reconstructed from experimental data show that most of these equilibria are very close to the marginal ballooning stability limit. This fact is also illustrated in Fig. 1 by plotting the value of the critical β_T to ideal modes, as parameterized by the General Atomic group.[9] The regime with $q_\psi > 3.5$, which is characterized by being very close to marginal ideal stability, having $\beta_p \geq 1.5$ and relatively low electron temperatures in

the confinement region, will be studied in detail. In this regime the plasma is particularly unstable to resistive ballooning modes.

In general, it will be shown that for modest poloidal beta, high current, and relatively high temperatures coupling to sound waves and compression has a significant stabilizing effect on low toroidal mode number instabilities. However, at high β_p (≥ 2), low current, and lower temperatures, the inclusion of coupling to sound waves has little effect on the predictions of the pressure convection model.

The equations studied and numerical techniques employed will be briefly described in the next section. The pressure convection model, relative to which the effects of compressibility are measured, will be discussed in Sec. III. In Sec. IV the effects of compressibility will be examined in detail, and conclusions will be drawn in Sec. V.

II. EQUATIONS

It is convenient to use an equilibrium coordinate system (ρ,θ,ϕ) in which the magnetic field lines are straight. Representing the equilibrium magnetic field as

$$\vec{B}_0 = F\vec{\nabla}\phi + \vec{\nabla}\phi \times \vec{\nabla}\psi \ , \tag{1}$$

where ϕ is the toroidal angle and $2\pi\psi$ is the poloidal flux, a flux coordinate system may be derived from the knowledge of ψ as a function of the Cartesian coordinates $X \equiv (R/R_0 - 1)$, Z. [Here X, Z are normalized to the value of the averaged minor radius (a)]. A straight field line system is determined by choosing the Jacobian as R^{-2}.[10,11] The variables ρ and θ then take the roles of the generalized radial and poloidal coordinates, respectively. In the normalized variables employed, ρ varies between 0 at the magnetic axis and 1 at the plasma edge.

Using an eikonal ballooning representation[12]

$$\vec{\xi}(\rho,\theta,\phi,t) = \sum_m e^{-im\theta} \int_{-\infty}^{\infty} e^{imy + in\lambda}\, \hat{\xi}(\rho,y,t)\, dy \ , \tag{2}$$

a set of equations to leading order in the toroidal mode number (n) is derived from the linearized resistive MHD equations. In the ρ, θ, and ϕ system of coordinates, the eikonal phase $\lambda = \phi - q(y - y_0)$ is particularly simple. For the equations to be consistent, it can be shown that $\vec{\nabla} \cdot \vec{V}_1 = 0$, to order n, and that the perturbed pressure balance must be maintained to highest order:

$$P_1 + \vec{B}_0 \cdot \vec{B}_1 = 0 \ , \tag{3}$$

where subscripts 0, 1 denote equilibrium and perturbed quantities respectively. To the next order in n, an expression for $\vec{\nabla} \cdot \vec{V}_1$ may be obtained from the component of the momentum equation parallel to the equilibrium magnetic field:

$$\vec{\nabla} \cdot \vec{V}_1 = -\frac{n^2 |\vec{\nabla}\lambda|^2}{B_0^2} \eta \vec{B}_0 \cdot \vec{B}_1 + \frac{\vec{B}_0}{B_0} \cdot \vec{\nabla} \left(\frac{\vec{B}_0}{B_0} \cdot \vec{V}_1 \right)$$

$$- \vec{V}_1 \cdot \left[\frac{\vec{B}_0}{B_0} \cdot \vec{\nabla} \left(\frac{\vec{B}_0}{B_0} \right) + \vec{\nabla} \ln B_0 \right] - \frac{1}{B_0^2} \frac{\partial}{\partial t} (\vec{B}_0 \cdot \vec{B}_1) \ . \tag{4}$$

It is convenient to normalize the variables. All lengths are normalized to

$$a = \left(\frac{R_0}{2\pi^2} \int R^{-2}\, dV \right)^{1/2} \ ,$$

an averaged plasma minor radius. The magnetic fields are normalized to the vacuum toroidal magnetic field at the magnetic axis ($B_{\xi 0}$); pressure, density, and resistivity are normalized to their equilibrium values at the magnetic axis (P_0, ρ_0, and η_0, respectively). Time is normalized to the poloidal Alfvén transit time, $\tau_{Hp} = R_0 \rho_0^{1/2}/B_{\xi 0}$. The inverse aspect ratio is given by $\epsilon = a/R_0$ and $S = \tau_{Hp}/\tau_R$, where τ_R is the resistive transit time $\tau_R = a^2/\eta_0$. Using the above relations and $\vec{\nabla} \cdot \vec{B}_1 = 0$, in normalized variables the projections of the momentum equation parallel to $\vec{B}_0$ and $\vec{\nabla}\rho$ are

$$\frac{\partial V_{\parallel}}{\partial t} = \frac{\beta_0}{2\epsilon} \frac{I}{B_0 R^2 q} \frac{\partial P_1}{\partial y} + \frac{q}{2\epsilon I B_0 \rho} \frac{\partial}{\partial \rho} (\beta_0 P_0)\ b_{\perp} , \tag{5}$$

$$\frac{\partial V_{\perp}}{\partial t} = \frac{P_1 q}{I\alpha} \frac{\beta_0}{2\epsilon^2} \left\{ \frac{1}{\rho} \frac{\partial}{\partial \rho} (\beta_0 P_0 + B_0^2) + \frac{I^2}{R^2 B_0^2} \left[\frac{\epsilon^2 g \rho \theta}{q^2} - \frac{q'}{\rho q} (y - y_0) \right] \frac{\partial B_0^2}{\partial y} \right\} - \frac{I B_0^2}{R^2 q \alpha} \frac{\partial}{\partial y} \left(\frac{\alpha b_{\perp}}{B_0^2} \right) . \tag{6}$$

The component of Ohm's law parallel to $\vec{\nabla}\rho$ is

$$\frac{\partial b_{\perp}}{\partial t} = - \frac{I}{R^2 q} \frac{\partial V_{\perp}}{\partial y} - \frac{\eta n^2}{S} \alpha\ b_{\perp} , \tag{7}$$

and the adiabatic pressure equation combined with Eqs. (3) and (4) yields

$$\left(1 + \frac{\beta_0}{2} \Gamma \frac{P_0}{B_0^2} \right) \frac{\partial P_1}{\partial t} = \frac{q}{\rho I} \frac{dP_0}{d\rho} V_{\perp} - \frac{\epsilon \Gamma I P_0}{B_0^2 R^2 q} \frac{\partial B_0}{\partial y} V_{\parallel}$$

$$- \frac{\Gamma P_0}{B_0^2} \left(\frac{\eta}{S} \frac{\beta_0}{2} n^2 \alpha P_1 - \frac{\epsilon I}{R^2 q} B_0 \frac{\partial V_{\parallel}}{\partial y} + \frac{q V_{\perp}}{I} \left\{ \frac{1}{\rho} \frac{\partial}{\partial \rho} \left(\frac{\beta_0}{2} P_0 + B_0^2 \right) \right.\right.$$

$$+\frac{I^2}{R^2B_0^2}\left[\frac{\epsilon^2 g^{\rho\theta}}{q^2}-\frac{q'(y-y_0)}{\rho q}\right]\frac{\partial B_0^2}{\partial y}\Bigg\}\Bigg) \qquad (8)$$

where $I = -F/(R_0B_{\xi 0})$, $V_\perp = \vec{V}_1 \cdot \vec{\nabla}\psi\, \tau_{Hp}/(a^2B_{\xi 0})$, $V_\parallel = \vec{V}_1 \cdot \vec{B}_0\tau_{Hp}/(aB_0)$, $b_\perp = \vec{b}_1 \cdot \vec{\nabla}\psi\, R_0/(a^2B_{\xi 0}^2)$, Γ is the ratio of specific heats, and $\alpha(\rho,y) = |\vec{\nabla}\lambda|^2$, which in this coordinate system is given by

$$\alpha(\rho,y) = \frac{\epsilon^2}{R^2}+\frac{q^2}{\rho^2}g^{\theta\theta}+\frac{2q'q}{\rho}(y-y_0)g^{\rho\theta}+q'^2(y-y_0)^2g^{\rho\rho}\ .$$

The content and physical interpretation of Eqs. (5) through (8) may be summarized as follows. Equation (6) is the radial momentum balance equation, where the effects of curvature drive and field line bending are opposed by inertia. Noting that Eq. (6) is equivalent to $\vec{\nabla}\cdot\vec{J} = 0$, where $\vec{\nabla}\cdot\vec{J} = \vec{\nabla}_\parallel\cdot\vec{J}_\parallel + (\vec{\nabla}_\perp\cdot\vec{J}_\perp)_{curv} + (\vec{\nabla}_\perp\cdot\vec{J}_\perp)_{inertia}$, it can be seen that field line bending corresponds to the parallel gradient of $\vec{J}_\parallel$ while the curvature and inertia terms contribute to $\vec{J}_\perp$. In Eq. (7), the Ohm's law relates $\vec{J}_\parallel$ to $\vec{E}_\parallel/\eta$, where $\vec{E}_\parallel$ is determined by inductive ($\partial b_\perp/\partial t$) and electrostatic ($\partial V_\perp/\partial y$) effects. Equation (8) is the parallel component of the $\vec{B}$ equation, where the adiabatic pressure evolution equation and perturbed pressure balance [Eq. (3)] have been used to eliminate $\vec{B}_0\cdot\vec{B}_1$ in terms of P_1. Hence, the right-hand side of Eq. (8) contains the terms corresponding to the effects of convection of pressure, compressional Alfvén wave propagation, and coupling to sound waves propagating along the magnetic field. Finally, Eq. (5) describes the evolution of $V_\parallel$.

Equations (5) through (8) are solved either as an initial value problem using a simple explicit numerical method or as an eigenvalue problem using a library boundary value routine.[13] The initial value approach is simple to use, and it is easy to include additional physics, such as diamagnetic effects, without any major coding alteration. The boundary value approach requires a good initial guess of the eigenvalue but permits tracking of the whole spectrum of

eigenvalues in the complex plane. Detailed tests of these codes, in the $\Gamma = 0$ limit, have been made by comparing their results to a boundary value code based on the equations of Ref. 2.

III. PRESSURE CONVECTION MODEL

In the pressure convection model limit ($\Gamma = 0$), Eqs. (6), (7), and (8) yield the following eigenvalue equation:

$$\frac{\partial}{\partial y}\left[\frac{\alpha}{\omega + \left(\frac{\eta n^2 \alpha}{S}\right)}\frac{\partial V_\perp}{\partial y}\right] - \frac{q^4}{\omega\rho}\frac{dP_0}{dp}\frac{\beta_0}{\epsilon}K(y)V_\perp - \omega q^2 \alpha V_\perp = 0 \ , \qquad (9)$$

where

$$K(y) = \frac{1}{\rho}\left(\frac{\partial X}{\partial \rho} - \frac{q'}{q}\, y\, \frac{\partial X}{\partial y}\right)$$

and $\omega = \gamma + i\omega_R$ (normalized to τ_{Hp}^{-1}), γ being the growth rate and ω_R being the real frequency. Small aspect ratio corrections are ignored to simplify matters. Equation (9) states that the effects of field line bending (first term) and inertia (third term) oppose the destabilizing curvature drive (second term). Note that the inclusion of resistivity ($\eta n^2 \alpha / S$) weakens the stabilizing effect of field line bending when $k_\perp^2$ ($= n^2\alpha$) becomes large. Hence, resistive ballooning modes are extended in y and may peak away from $y = 0$, at y values corresponding to large radial wave numbers. Figure 2 shows typical eigenfunctions of $V_\perp$, in the incompressible limit, for three equilibria with increasing poloidal betas (β_p). The $\beta_p = 1.29$ equilibrium is computed to match experimental measurements from ISX-B.[8,14] The other two equilibria used for Fig. 2 are derived from the $\beta_p = 1.29$ equilibrium, by multiplying the pressure profile by a constant. The highest poloidal beta equilibria ($\beta_p = 1.88$) is ideally unstable. The eigenfunctions in Fig. 2 show that as the equilibria become increasingly ideally stable, so the mode has to extend further to overcome the influence of the field line bending term. In real space

this corresponds to modes becoming radially localized and thus requiring less energy for the interchange of field lines. Figure 3 shows how the eigenfunction structure varies as a function of toroidal mode number (n) for the $\beta_p = 1.29$ equilibrium. For the incompressible resistive ballooning mode, the effects of varying resistivity or toroidal mode number are described by the single parameter $\eta n^2/S$. Hence, Fig. 3 shows that as n increases, or equivalently η/S increases, the mode has to extend less in y to overcome the influence of the field line bending term. The reason for this is that the resistivity allows slippage between the field lines and fluid; thus, as $\eta n^2/S$ increases the mode has to extend less in ballooning space, or equivalently become less radially localized in real space, to make the interchange of field lines energetically possible.

Equation (9) may be solved approximately using a two-length scale expansion[15] and a shifted circle approximation for the equilibrium

$$X = X_0 + \rho \cos\theta \quad , \quad Z = \rho \sin\theta \; . \tag{10}$$

Defining $D_0 = dX_0/d\rho$, then to order D_0 the equilibrium quantities in Eq. (9) are

$$\begin{aligned} \alpha(\rho,y) &= \frac{q^2}{\rho^2}\left[1 + \hat{S}^2y^2 + 2D_0(\cos y + \hat{S}y \sin y)\right] , \\ K(\rho,y) &= \frac{1}{\rho}(D_0 + \cos y + \hat{S}y \sin y) , \end{aligned} \tag{11}$$

where $\hat{S} = \rho q'/q$ is the shear parameter. Using these analytic approximation equations, Eq. (9) becomes

$$a_r\omega \frac{\partial}{\partial y}\left[\frac{1 + \hat{S}^2y^2 + 2D_0(\cos y + \hat{S}y \sin y)}{1 + \hat{S}^2y^2 + q^2a_r\omega + 2D_0(\cos y + \hat{S}y \sin y)} \frac{\partial V_\perp}{\partial y}\right]$$

$$- \omega^2 \left[1 + \hat{S}^2 y^2 + 2D_0(\cos y + \hat{S} y \sin y)\right] V_\perp$$

$$+ 2u(D_0 + \cos y + \hat{S} y \sin y) V_\perp = 0 \ , \tag{12}$$

where $u = (-\beta_0/2\epsilon)(dP_0/d\rho)$ and $a_r = (\rho^2/q^4)(S/\eta n^2)$. It is convenient to remove the first derivative in Eq. (12) by using the transformation

$$V_\perp = \left[1 + \frac{q^2 a_r \omega}{1 + \hat{S}^2 y^2 + 2D_0(\cos y + \hat{S} y \sin y)}\right]^{-1/2} W \ . \tag{13}$$

Expanding to first order in D_0, Eq. (12) then becomes

$$a_r \omega \frac{d^2 W}{dy^2} + [r(y) + s(y)\sin y + c(y)\cos y] W = 0 \ , \tag{14}$$

where details of the coefficients r, s, and c are given in the appendix. Equation (14) may be solved approximately using a two-length scale expansion

$$W(y) = W_0(y) + W_c(y)\cos y + W_s(y)\sin y \ , \tag{15}$$

where all the rapid fluctuations of length scale 2π are contained in the trigonometric terms and W_0, W_c, W_s are broad envelope functions. Substituting Eq. (15) into Eq. (14) and equating terms yields

$$W_s = \frac{s\, W_0}{a_r \omega - r} \ , \tag{16}$$

$$W_c = \frac{c\, W_0}{a_r \omega - r} \ , \tag{17}$$

and the averaged part combined with these equations gives

$$a_r\omega \frac{d^2W_0}{dy^2} + r(y)W_0 + \frac{s(y)^2 + c(y)^2}{2[a_r\omega - r(y)]} W_0 = 0 \ . \tag{18}$$

Figure 4 compares the $V_\perp$ eigenfunctions obtained by numerical boundary value solutions of Eq. (9), Eq. (18), and the full equations with no aspect ratio ordering. Two sets of eigenfunctions for large aspect ratio ($\epsilon = 0.1$) and small aspect ratio ($\epsilon = 0.33$) are shown. The eigenfunctions obtained from the solution of Eq. (18) are reconstructed using Eqs. (15) through (17). Numerical equilibria were used for the full and reduced equation solutions shown in Fig. 4. The eigenfunctions always agree reasonably well in width, but at small aspect ratios the details of the eigenfunction do not agree so well. This disagreement is primarily due to the use of a shifted circle approximation to the real equilibrium. The width of the mode is determined by the balance of field line bending with inertia at large y. Hence, the width L is given by

$$L = \left(\frac{\eta n^2}{4S} \omega q^2 q'^2\right)^{-1/4} \ . \tag{19}$$

It is interesting to note that the width of the mode along y, the extended poloidal coordinate, is effectively the reciprocal of the resistive layer width determined by Coppi, Greene, and Johnson.[16] Hence, the two-scale expansion separates $k_\parallel$ into a fast scale 1/Rq and a slow scale 1/RqL. These correspond to radial scales Δ and λ_r, where $\Delta = (nq\hat{S}/\rho)^{-1}$, the spatial separation of poloidal harmonics at fixed n, and $\lambda_r = \rho/Lnq\hat{S}$, the resistive layer thickness. In light of this interpretation of the scales, it is instructive to note that the destabilizing effect in Eq. (18) can be traced to the slow-scale average of the product of the fast-scale geodesic curvature and the

pressure fluctuation. Hence, it may be said that the resistive ballooning mode is driven by geodesic curvature.

Further analytic progress may be made by ignoring the average well ($D_0 = 0$) and making an electrostatic approximation. The electrostatic approximation is valid at large y, where the mode envelope peaks in the region in which field line bending is weakened by resistivity. With these approximations Eq. (18) reduces to

$$\frac{d^2W_0}{dy^2} + \frac{(1 + \hat{S}^2y^2)[2u^2 - a_r\omega^3 - \omega^4(1 + \hat{S}^2y^2)]}{a_r\omega[a_r\omega + \omega^2(1 + \hat{S}^2y^2)]} W_0 = 0 \ . \tag{20}$$

Equation (20) is a potential equation, for which a necessary condition for a solution with adequate boundary conditions at $y = \pm\infty$ is that the potential be negative in some interval. Therefore, equating the coefficient of $\hat{S}^2y^2$ to zero yields the dispersion relation

$$\omega^2(2\omega^2 + a_r\omega) = 2u^2 \ . \tag{21}$$

In the limit $\omega << a_r/2$ this dispersion relation yields a pure growing mode, with growth rate

$$\gamma = \left(\frac{2u^2}{a_r}\right)^{1/3} = \left(\frac{\beta_0}{\epsilon}\frac{q^2}{\rho}\frac{dP_0}{d\rho}\right)^{2/3}\left(\frac{\eta n^2}{2S}\right)^{1/3} \ . \tag{22}$$

These modes were considered in Ref. 6, where a nonlinear theory is discussed. Figure 5 shows a comparison of this dispersion relation [Eq. (21)] with numerical solutions of Eq. (18) and of the full and reduced ballooning equations. The reduced equations are those obtained from Eqs. (6), (7), and (8) by ignoring small aspect ratio corrections. In real space these equations are the reduced high beta tokamak equations.[17] Reasonable quantitative agreement is displayed in Fig. 5

at low n. At larger values of $\eta n^2/S$ the mode becomes more localized about $y = 0$, and the multiple-scale length approximation breaks down. This is responsible for the discrepancy at large n in Fig. 5. The regime in which the growth rate has no dependence on toroidal mode number (or resistivity) is termed the fast ballooning limit, by analogy with the Coppi, Greene, and Johnson fast interchange limit.[16]

Ideal modes that tend to be very localized, in ballooning space, about $y = 0$ are sensitive to their parity at $y = 0$ and to the value of the radial wave number (y_0). Resistive ballooning modes that are very extended in ballooning space show little dependence on these factors. Figure 6 shows how the growth rate varies as a function of y_0 for the $\beta_p = 1.29$ equilibria mentioned above. The $n = 5$ curve corresponds to a very extended mode, and the growth rate appears practically degenerate in y_0. The $n = 20$ mode is localized about $y = 0$ and, as an ideal mode, has a maximum in its growth rate for $y_0 = 0$. In the next section, it will be shown that modes which are very extended are completely, or almost completely, stabilized by compressibility effects, whereas modes localized about $y = 0$ are affected to a much lesser extent. Hence, the dominant modes when compressibility effects are taken into account have even parity in $V_\perp$ and $y_0 = 0$.

The limit of validity for the reduced high beta tokamak equations has been investigated for the convective pressure model. Figure 7 shows the growth rate as a function of radius for the three varying beta equilibria used in Fig. 2. For the low poloidal beta case ($\beta_p = 0.91$) the full and reduced equations agree well. However, at higher poloidal betas, as the ordering assumptions used in deriving the reduced equations are violated, the agreement deteriorates. For these values of β_p the full MHD equations give larger linear growth rates.

IV. COMPRESSIBILITY EFFECTS

Equations (5) through (8) may be reduced to the coupled eigenvalue equations:

$$\frac{1}{q^2}\frac{\partial}{\partial y}\left[\frac{\alpha}{1+\left(\frac{\eta n^2}{\omega S}\right)\alpha}\frac{\partial V_\perp}{\partial y}\right] - \omega^2\alpha V_\perp - q\frac{\beta_0}{\epsilon}\omega K(y)P_1 = 0 , \tag{23}$$

$$\left(1-\frac{\omega_s^2}{\omega^2}\frac{\partial^2}{\partial y^2}\right)\omega P_1 = \frac{q}{\rho}\frac{dP_0}{d\rho}V_\perp - \frac{\beta_0\Gamma P_0}{2\omega\rho q}\frac{dP_0}{d\rho}\frac{\partial}{\partial y}\left[\frac{1}{\omega+\left(\frac{\eta n^2\alpha}{S}\right)}\frac{\partial V_\perp}{\partial y}\right]$$

$$+ 2\epsilon\Gamma P_0 q K(y)V_\perp - \frac{\Gamma P_0\eta}{S}\frac{\beta_0}{2}n^2\alpha P_1 , \tag{24}$$

where small aspect ratio corrections are ignored. Here $\omega_s^2 = \beta_0\Gamma P_0/2q^2$ is the sound frequency. Equations (23) and (24) may again be solved by a two-length scales approach. Using a shifted circle equilibria with $D_0 = 0$ and making an electrostatic approximation, the following eigenvalue equation is obtained for the slow scale:

$$a_r\omega\frac{d^2V_0}{dy^2} - (1+\hat{S}^2y^2)\omega^2V_0 + \frac{u(1+\hat{S}^2y^2)}{\left[1+\frac{\omega_s^2}{\omega^2}+\frac{\omega_s^2}{a_r\omega}(1+\hat{S}^2y^2)\right]}$$

$$\times\left\{\frac{2u}{\left[a_r\omega+\omega^2(1+\hat{S}^2y^2)\right]\left[1+\frac{\omega_s^2}{a_r\omega}(1+\hat{S}^2y^2)\right]+2\omega_c^2(1+\hat{S}^2y^2)} - \frac{2\omega_c^2}{u}\right\}V_0$$

$$= 0 , \tag{25}$$

where $\omega_c^2 = q^2\omega_s^2$.

Some insight into the principal effects of compressibility may be gained by consideration of a simplified version of Eq. (25). By noting $a_r \gg \omega$, ω_c, and ω_s and considering extended modes, Eq. (25) can be simplified to

$$a_r\omega \frac{d^2V_0}{dy^2} - (1 + \hat{S}^2y^2)\omega^2V_0 + \frac{u(1 + \hat{S}^2y^2)}{(1 + \omega_s^2/\omega^2)}\left(\frac{2u}{a_r\omega} - \frac{2\omega_c^2}{u}\right)V_0 = 0 \ . \qquad (26)$$

In the limit $\omega_s = \omega_c = 0$, Eq. (26) reduces to the $a_r \gg \omega$ limit of Eq. (20). It is apparent that there are two compression effects. The first, associated with ω_s, is due to coupling to the parallel sound wave [$\vec{\nabla}_{\parallel}V_{\parallel}$ in Eq. (8)]. When $\omega_s/\omega \to \infty$, the pressure-driving term vanishes because under such conditions the fast-scale pressure fluctuation tends to isobarize along y. Hence, $\vec{B} \cdot \vec{\nabla}P = 0$ and $P_1 \simeq (B_1^o dP_o/d\rho)/(B_o n)$. However, at large y resistive diffusion forces $B_1^o \approx 0$, and thus $P_1 \approx 0$, which destroys the instability drive. It should be noted that in the case of isobaric fast-scale pressure fluctuations, instabilities with growth rates scaling as $\gamma \sim \eta^{3/5}$ persist.[15] However, such instabilities do not tap free expansion energy at a rate sufficient to be of relevance to transport in ISX-B. Modes with $\omega > \omega_s$ are not affected much by parallel compression. The second effect, associated with ω_c, is due to compression across the magnetic field [$\vec{V} \cdot \vec{\nabla}B_0$ in Eq. (8)] and the necessity of balance of plasma and magnetic compression as given in Eq. (3). The perpendicular compression effects enter secularly, as y^2, due to the beating of oscillatory curvature terms in Eqs. (8) and (6). For $\omega_c \geq \omega$, perpendicular compression replaces inertia in the balance with pressure drive, thus drastically reducing the growth rate to resistive diffusion time scales. For $\omega_c < \omega$, perpendicular compression has little effect and the pressure convection model is recovered. Note that, since $q \geq 1$ in the region of interest, perpendicular compression is the most important effect associated with finite Γ. Finally, it is interesting to observe that perpendicular compression appears in kinetic treatments

from the expansion to first order of the pressure-driving terms in ω_D/ω, where ω_D is the magnetic drift frequency.

An approximate dispersion relation solution of Eq. (25) is

$$2\omega^4 + \left(a_r + \frac{6\omega_s^2}{a_r}\right)\omega^3 + \left(6\omega_s^2 + 8\omega_c^2 + \frac{4\omega_s^4}{a_r^2}\right)\omega^2 + \left[a_r(\omega_s^2 + 2\omega_c^2) + \frac{6\omega_s^2}{a_r}(\omega_s^2 + 2\omega_c^2)\right]\omega$$

$$+ 2(\omega_s^2 + 2\omega_c^2)^2 = 2u^2 \quad . \tag{27}$$

In the limit $\omega \gg \omega_c$ (and therefore $\omega \gg \omega_s$, since $q > 1$ in the region of interest), the dispersion relation Eq. (27) reduces to the incompressible limit [Eq. (21)], and thus compressibility has little effect, as discussed above. In the other limit of practical interest $\omega a_r \gg \omega_c^2$, $\omega \ll \omega_s$, ω_c and ignoring inertia effects, which are only important at very high n, Eq. (27) reduces to

$$a_r\omega(\omega_s^2 + 2\omega_c^2) = 2u^2 \quad . \tag{28}$$

In this limit the growth rate scales linearly with the resistivity and is greatly reduced by the compressibility effects. Also, since $q > 1$ the stabilizing influence of the perpendicular compressibility will always dominate that of the parallel dynamics. The parallel dynamics limit ($\omega_c = 0$) has been considered previously.[18]

These results are borne out by the numerical solutions of Eqs. (5) through (8) for parameters relevant to ISX-B. The shots corresponding to the $\beta_p = 1.29$ equilibria, used in Fig. 2, have a magnetic Reynolds number $S \simeq 2.1 \times 10^6$. Using this value and a flux surface average of a resistivity that would maintain a resistive equilibrium, Fig. 8 shows the growth rate as a function of toroidal mode number in the limits $\Gamma = 0$ and $\Gamma = 5/3$ for two flux surfaces. Also indicated on the figure are the separate contributions from the parallel and perpendicular compressibility. The perpendicular effects dominate, as the dispersion

relation indicates. The reason that the compressibility has less effect on the outer surfaces is that the growth rate changes slowly with radius, whereas $\omega_c(\alpha P_0)$ decreases with radius. Figure 9 shows the dispersion relation solution corresponding to the lower graph of Fig. 8. The relative importance of the parallel and perpendicular compressibility is resolved, but exact quantitative agreement is not achieved.

One effect not resolved by the dispersion relation is that of overstability. In the regime where the compressibility completely, or almost completely, stabilizes the mode, the numerical solution is overstable. Using the initial value approach to solve Eqs. (5) through (8), the overstability is manifested by the dependent variables ($b_\perp$, $V_\perp$, P_1) oscillating with a fixed period. Using the boundary value approach, the overstability corresponds to complex eigenvalues. Figure 10 traces the roots in the complex plane as a function of toroidal mode number for the flux surfaces and parameters as Fig. 8. The particular branches traced in Fig. 10 are continuations of the fastest growing compressible branches shown in Fig. 8; various other branches exist.[19]

Equilibria reconstructed from high poloidal beta ($\beta_p \gtrsim 2$) shots on ISX-B using the methods of Ref. 14 are not available. Instead, numerical equilibria that approximately match experimental conditions and are just ideally stable are used. In particular, an equilibrium with the q value varying between 0.9 on axis and 7.0 at the edge and with $\beta_p = 2.0$ will be considered. Since the electron temperatures in ISX-B are lower for shots of this type, a correspondingly lower magnetic Reynolds number $S = 10^6$ is used. Figure 11 shows how the compressibility effects vary for the numerical solution and dispersion relations, between the $\rho = 0.4$ and 0.7 surfaces. Good qualitative agreement can be seen between the dispersion relation and numerical solution. Figure 12 traces the compressible roots in the complex plane for the same flux surfaces and parameters as Fig. 11. Comparing the results of this equilibrium with those of the $\beta_p = 1.29$ equilibrium shows that at higher β_p and lower temperature (larger η) the compressibility has less effect. This is because the growth rates rise

in the pressure convection limit with η and β_p, and so the regime $\omega > \omega_c$ is more easily attained. When the modes become overstable, their growth rates have been greatly reduced by the effects of compressibility. Hence the maximum toroidal mode number for overstability (n_{crit}) provides a good means of quantifying the compressibility effects. Figure 13 shows n_{crit} as a function of radius for the $\beta_p = 1.29$ and 2.0 equilibria. The compressibility effects can again be seen to be less important at high β_p and low temperatures.

V. CONCLUSIONS

The effects of compressibility on the resistive ballooning mode have been assessed for situations relevant to ISX-B. The pressure convection model predicts a resistive ballooning instability with growth rate

$$\gamma = \left(\frac{\beta_0}{\epsilon}\frac{q^2}{\rho}\frac{dP_0}{d\rho}\right)^{2/3}\left(\frac{\eta n^2}{2S}\right)^{1/3} .$$

The full MHD equations are studied to understand the stabilizing effects of compression and to determine the validity of the pressure convection model. At high current, modest β_p ($\sim$1), and relatively high temperature, the stabilizing influence of the compressibility is quite large and can completely, or almost completely, stabilize low toroidal mode number modes. However, at higher β_p ($\sim$2) and lower temperatures, the compressibility has much less effect and imposes little restriction on the unstable wave numbers predicted by the pressure convection model for the outer surfaces.

ACKNOWLEDGMENTS

We would like to acknowledge many useful discussions with M. N. Rosenbluth and stimulating criticism from A. H. Glasser. We also should like to thank M. Murakami and J. L. Dunlap for providing us with experimental results and L. A. Charlton for providing some of the equilibria used in this study.

This research was sponsored by the Office of Fusion Energy, U.S. Department of Energy, under Contract No. W-7405-eng-26 with the Union Carbide Corporation and by contract DOE/ET/53088 with the Institute for Fusion Studies.

APPENDIX

The functions used in Eq. (14) are:

$$r(y) = \frac{a_r^3\omega^3\hat{S}^4y^2q^4}{v^2(1+\hat{S}^2y^2)^2} - \frac{\hat{S}^2q^2a_r^2\omega^2}{v(1+\hat{S}^2y^2)}\left(1 - \frac{4y^2\hat{S}^2}{v}\right)$$

$$- \omega^2 v + 2uD_0 ,$$

$$s(y) = \frac{\hat{S}^2yq^4a_r^3\omega^3}{v^3(1+\hat{S}^2y^2)^2}\left[2vD_0(\hat{S}-1) - 8\hat{S}^3y^2D_0 - \frac{4D_0q^2a_r\omega\hat{S}^3y^2}{1+\hat{S}^2y^2}\right]$$

$$- \frac{D_0q^2a_r^2\omega^2}{v(1+\hat{S}^2y^2)}\left(-\hat{S}y - \frac{8\hat{S}^2y}{v}(\hat{S}-1) - \frac{4\hat{S}^3y}{v} + \frac{24\hat{S}^5y^3}{v^2}\right)$$

$$+ \frac{2D_0q^4a_r^3\omega^3\hat{S}^3y}{v^2(1+\hat{S}^2y^2)^2}\left(1 - \frac{4\hat{S}^2y^2}{v}\right)$$

$$- 2D_0\hat{S}y\omega^2 + \frac{2uv\hat{S}y}{1+\hat{S}^2y^2} ,$$

$$c(y) = \frac{\hat{S}^3y^2q^4a_r^3\omega^3D_0}{v^3(1+\hat{S}^2y^2)^2}\left(2v - 8\hat{S} - \frac{4q^2a_r\omega\hat{S}}{1+\hat{S}^2y^2}\right)$$

$$- \frac{D_0q^2a_r^2\omega^2}{v(1+\hat{S}^2y^2)}\left(2\hat{S} - 1 - \frac{8\hat{S}^3y^2}{v} - \frac{4\hat{S}^2}{v} + \frac{24\hat{S}^4y^2}{v^2}\right)$$

$$+ \frac{2D_0 q^4 a_r^3 \omega^3 \hat{S}^2}{v^2(1 + \hat{S}^2 y^2)^2} \left(1 - \frac{4\hat{S}^2 y^2}{v}\right)$$

$$- 2D_0\omega^2 + \frac{2uv}{1 + \hat{S}^2 y^2}$$

where

$$v = 1 + \hat{S}^2 y^2 + q^2 a_r \omega \ .$$

REFERENCES

[1]H. P. Furth, J. Killeen, M. N. Rosenbluth, and B. Coppi, in Plasma Physics and Controlled Nuclear Fusion Research (IAEA ,Vienna, 1966), Vol. 1, p. 103.

[2]G. Bateman and D. B. Nelson, Phys. Rev. Lett. 41, 1809 (1978).

[3]B. B. Kadomstev, O. P. Pogutse, and E. I. Yurchenko, in Plasma Physics and Controlled Nuclear Fusion Research, (IAEA, Vienna, 1983), Vol. 3.

[4]V. M. Gribkov, D. Kh. Morozov, O. P. Pogutse, and E. I. Yurcherko, in Plasma Physics and Controlled Nuclear Fusion Research (IAEA, Vienna, 1981), Vol. 1, p. 571.

[5]M. S. Chance, R. L. Dewar, E. A. Frieman, A. H. Glasser, J. M. Greene, R. C. Grimm, S. C. Jardin, J. L. Johnson, J. Manickan, M. Okabayashi, and A. M. M. Todd, in Plasma Physics and Controlled Nuclear Fusion Research (IAEA, Vienna, 1979), Vol. 1, p. 677.

[6]B. A. Carreras, P. H. Diamond, M. Murakami, J. L. Dunlap, J. D. Bell, H. R. Hicks, J. A. Holmes, E. A. Lazarus, V. K. Paré, P. Similon, C. E. Thomas, and R. M. Wieland, Phys. Rev. Lett. 50, 503–506 (1983).

[7]H. C. Howe, Bull. Am. Phys. Soc. 27 (8), Part II, 1014, paper 5D3 (1982).

[8]L. A. Charlton, G. H. Neilson, and R. M. Wieland (submitted to Phys. Fluids).

[9]L. C. Bernard, F. J. Helton, R. W. Moore, and T. N. Todd, "MHD beta limit scaling laws and comparison with Doublet III," General Atomic Report GA-A16981 (1983).

[10]R. L. Dewar, J. Manickam, R. D. Grimm, M. S. Chance, Princeton Plasma Physics Laboratory Report 1663 (1980).

[11]V. E. Lynch, B. A. Carreras, J. A. Holmes, H. R. Hicks, and L. Garcia, Comp. Phys. Com. 24 (81), 465 (1981).

[12]J. W. Connor, R. J. Hastie, and J. B. Taylor, in Plasma Physics and Controlled Nuclear Fusion Research (IAEA, Vienna, 1978), Vol. 1, p. 667.

[13]M. E. Lord, M. R. Scott, and H. A. Watts, Applied Nonlinear Analysis, (Academic, New York, 1979), pp. 635-656.

[14]R. M. Wieland, H. C. Howe, E. A. Lazarus, M. Murakami, and C. E. Thomas, Nucl. Fusion 23, 447 (1983).

[15]H. R. Strauss, Phys. Fluids 24, 2004 (1981).

[16]B. Coppi, J. M. Greene, and J. L. Johnson, Nucl. Fusion 6, 1001 (1966).

[17]H. R. Strauss, Phys. Fluids 20 1354 (1977).

[18]B. A. Carreras, J. L. Dunlap, W. A. Cooper, R. A. Dory, T. C. Hender, M. Murakami, V. K. Paré, A. J. Wootton, J. D. Bell, L. A. Charlton, H. R. Hicks, J. A. Holmes, V. E. Lynch, R. M. Wieland, P. H. Diamond, and P. L. Similon, Oak Ridge National Laboratory Report ORNL/TM-8648, 1983.

[19]A. H. Glasser, M. S. Chance, and R. L. Dewar, in Proceedings of 9th European Conference on Controlled Fusion and Plasma Physics, Oxford, 1979, paper A3.1.

FIGURE CAPTIONS

Fig. 1 Electron temperature at half radius and toroidal beta (β_T) as a function of q edge for two fixed beam power scans on ISX-B.

Fig. 2 Variation in ballooning mode eigenfunction structure of $V_\perp$ for three equilibria with differing poloidal betas ($\eta n^2/S = 10^{-3}$).

Fig. 3 Variation in eigenfunction structure with toroidal mode number (n) for $\beta_p = 1.29$ equilibria of Fig. 2 ($\eta/S = 10^{-5}$).

Fig. 4 Comparison of $V_\perp$ eigenfunctions from numerical and two-length scale solutions for large and small aspect ratio equilibrium.

Fig. 5 Comparison of dispersion relation, two-scale length solution, and numerical solutions for large aspect ratio equilibrium.

Fig. 6 Variation of growth rate with radial wave number (y_0) for n = 5 and 20 ($\beta_p = 1.29$, $\eta/S = 10^{-5}$).

Fig. 7 Comparison of growth rates as a function of radius between full (solid lines) and reduced (broken lines) ballooning equations for the three equilibria used in Fig. 2 ($\eta n^2/S = 4 \times 10^{-4}$).

Fig. 8 Growth rates as a function of toroidal mode number for two flux surfaces $\rho = 0.4$, 0.8 ($\beta_p = 1.29$). The effects of compressibility ($\Gamma = 5/3$) and the contributions of parallel and perpendicular compressibility are shown.

Fig. 9 Dispersion relation solution corresponding to the lower plot of Fig. 8.

Fig. 10 Complex eigenvalues for same flux surfaces and equilibria as Fig. 8. Arrows show the direction of decreasing toroidal mode number (indicated numbers are toroidal mode numbers).

Fig. 11 Comparison of numerical solutions and dispersion relation at $\rho = 0.4$ and 0.7 for high β_p case ($\beta_p = 2.0$).

Fig. 12 Complex eigenvalues for same flux surfaces and equilibria as Fig. 11. Arrows show the direction of decreasing toroidal mode number (indicated numbers are toroidal mode numbers).

Fig. 13 Minimum toroidal mode number for pure growing mode (n_{crit}) as a function of radius for $\beta_p = 1.29$ and 2.0 equilibria.

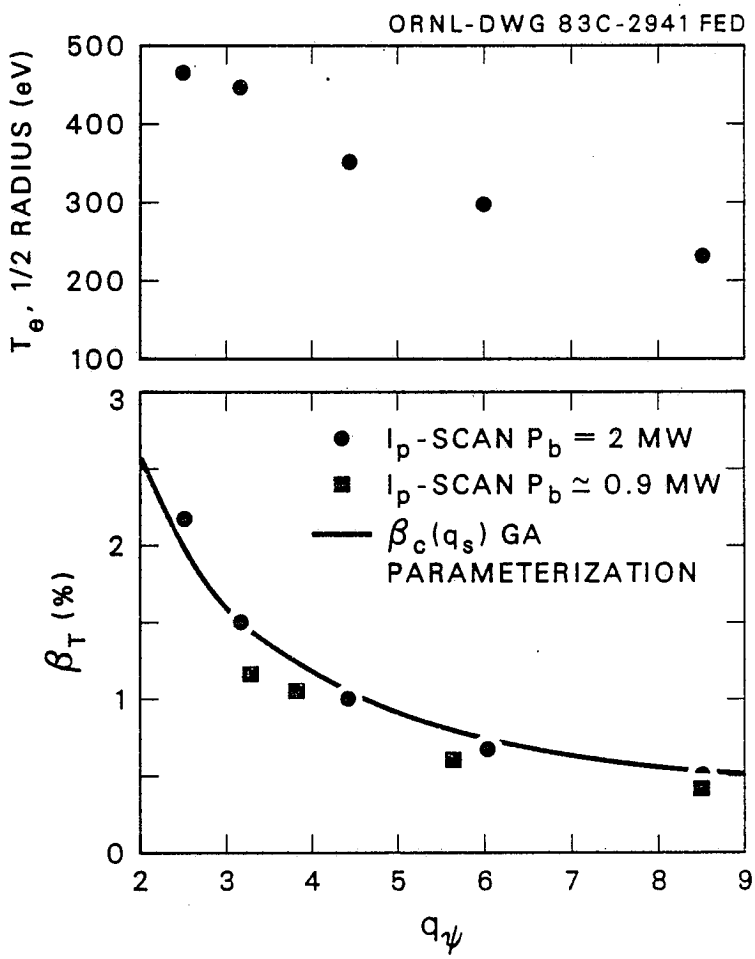
ORNL-DWG 83C-2941 FED
T_e, 1/2 RADIUS (eV)
500
400
300
200
100
3
2
1
0
β_T (%)
I_p-SCAN P_b = 2 MW
I_p-SCAN $P_b \simeq$ 0.9 MW
$\beta_c(q_s)$ GA PARAMETERIZATION
2
3
4
5
6
7
8
9
q_ψ

Fig. 1

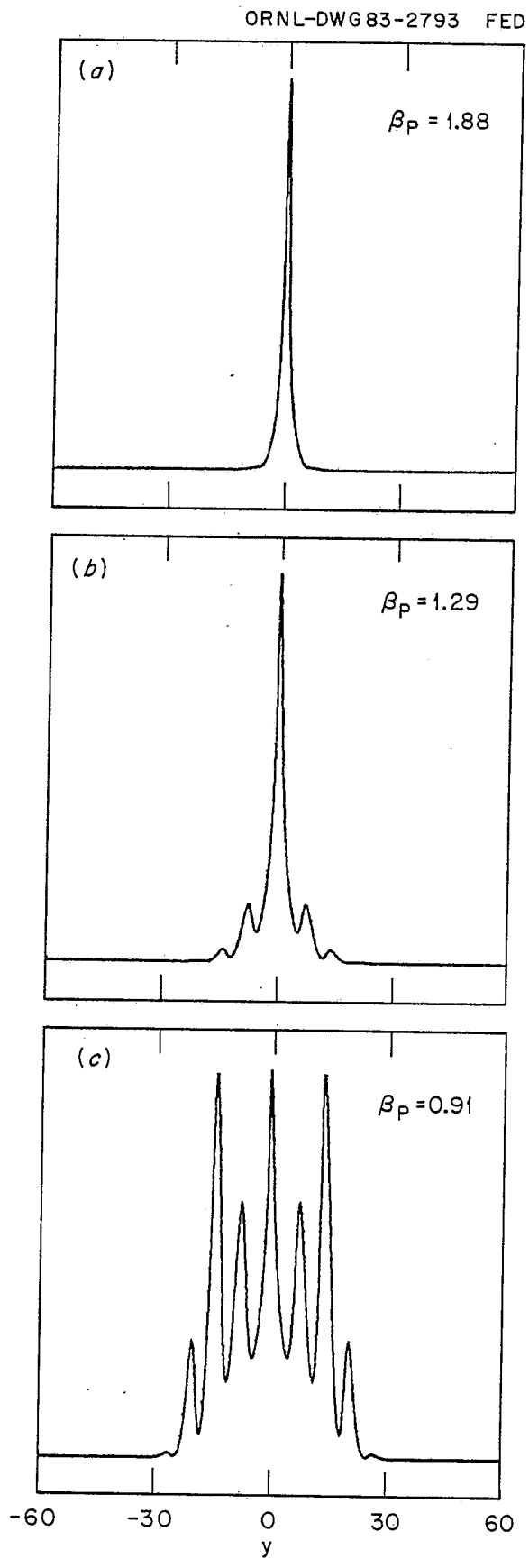
ORNL-DWG 83-2793 FED
(a)
β_P = 1.88
(b)
β_P = 1.29
(c)
β_P = 0.91
-60
-30
0
30
60
y

Fig. 2

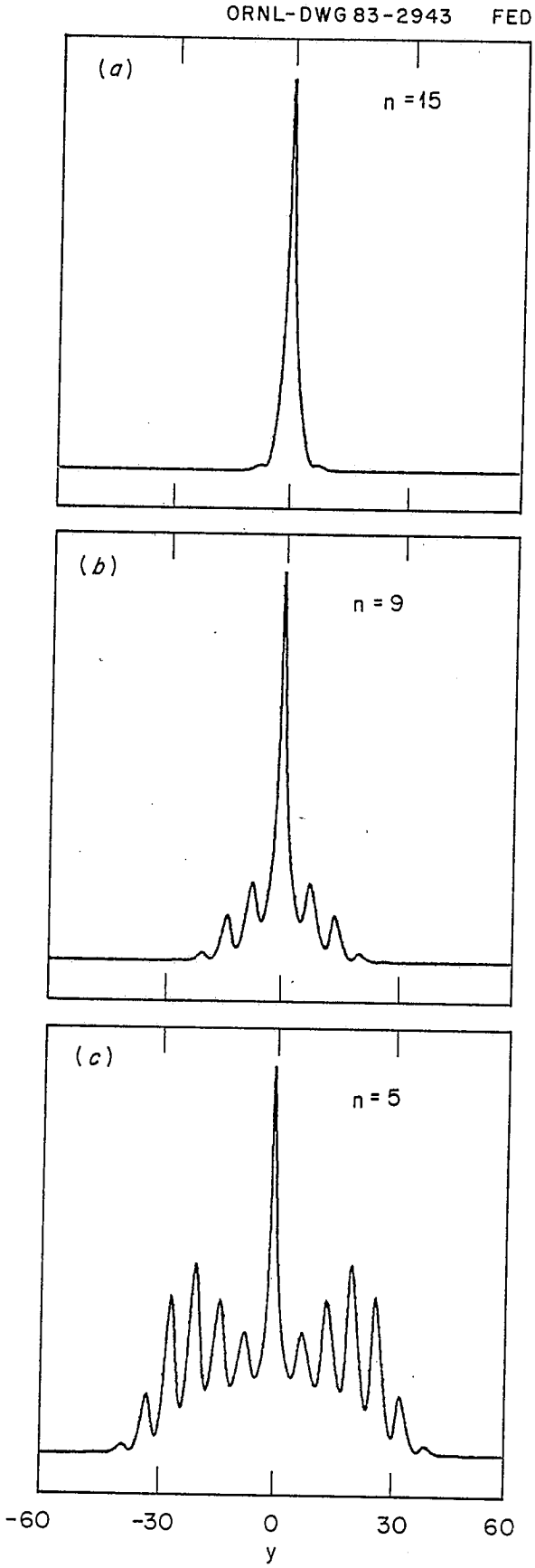

Fig. 3

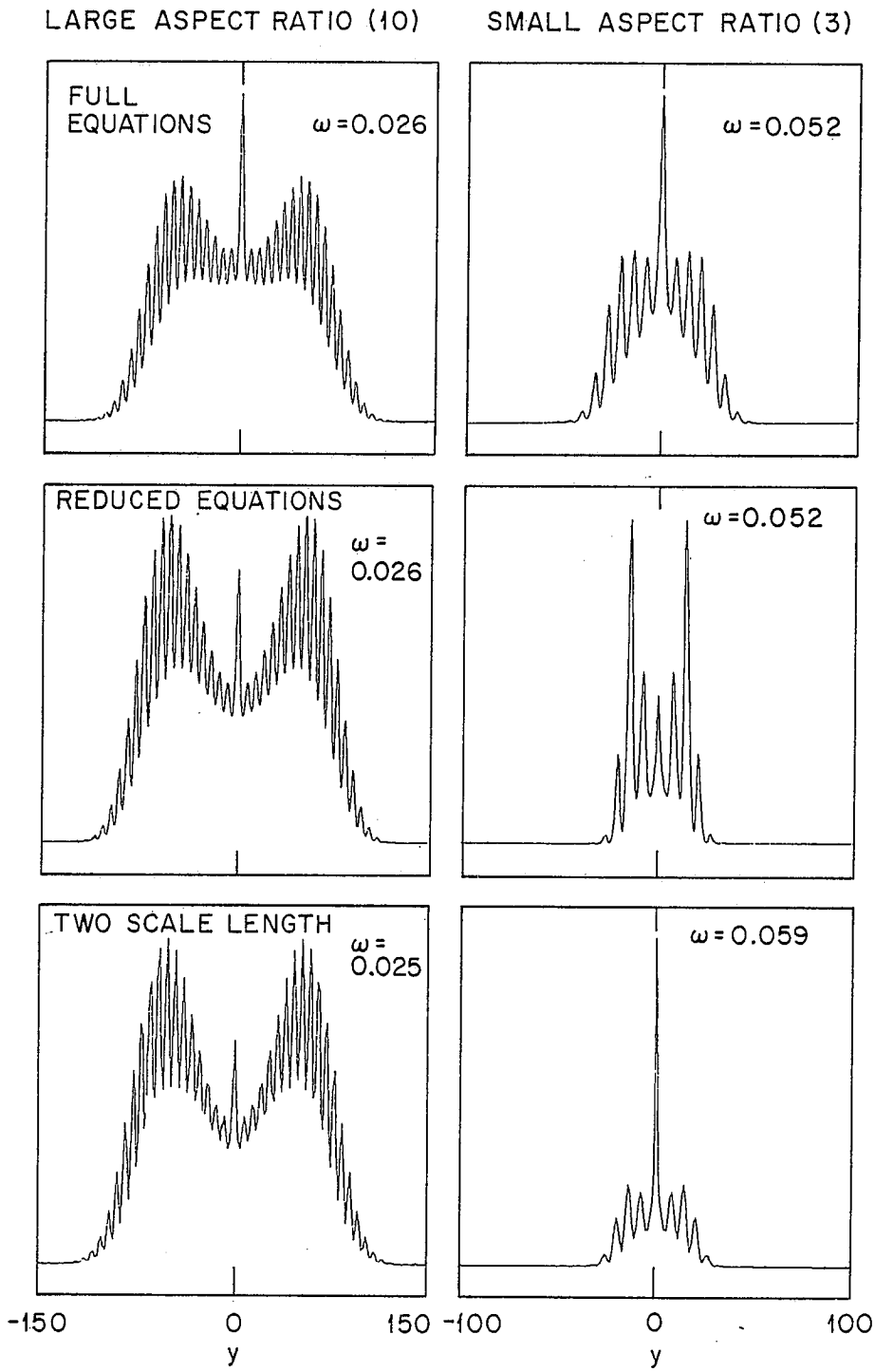
LARGE ASPECT RATIO (10)
SMALL ASPECT RATIO (3)
FULL EQUATIONS
ω=0.026
ω=0.052
REDUCED EQUATIONS
ω= 0.026
ω=0.052
TWO SCALE LENGTH
ω= 0.025
ω=0.059
-150
0
150
-100
0
100
y
y

Fig. 4

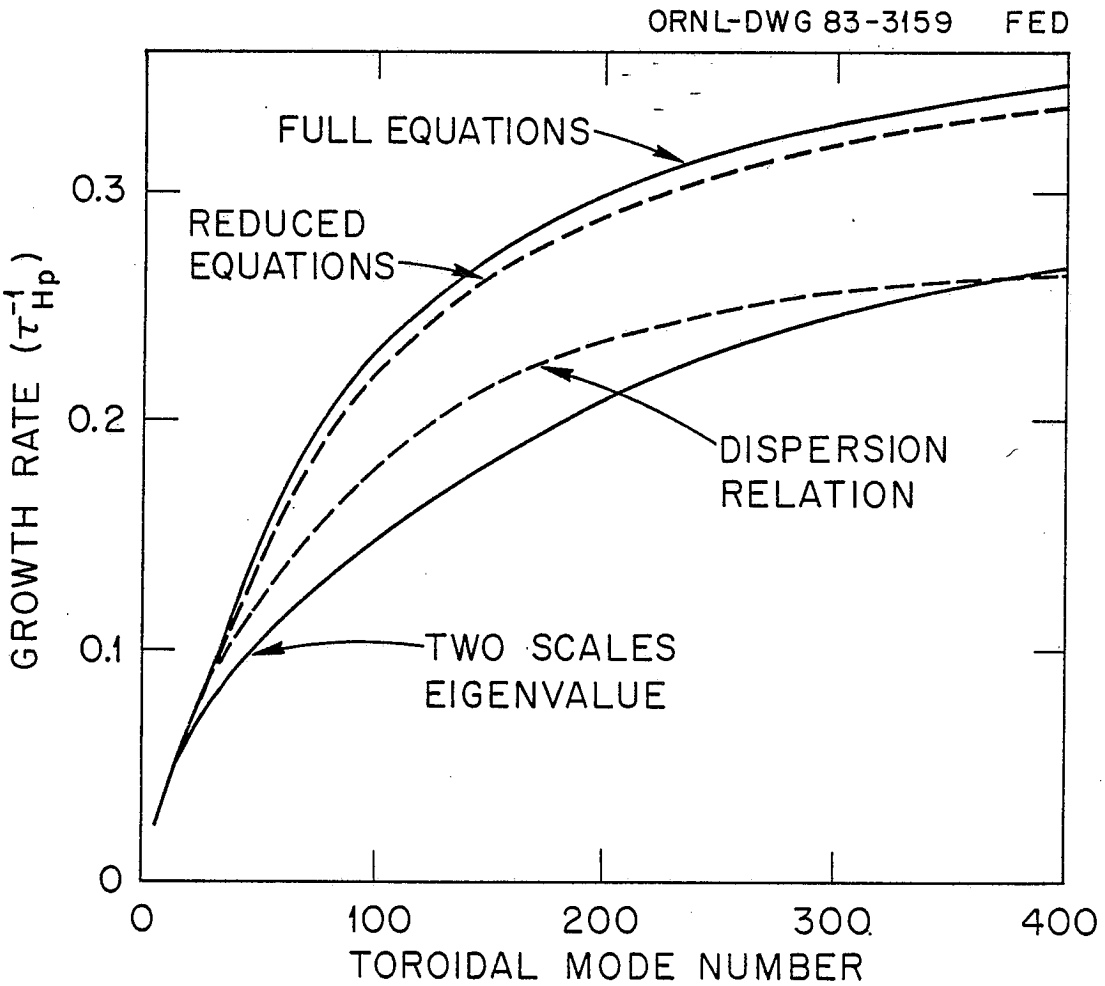
ORNL-DWG 83-3159 FED
FULL EQUATIONS
REDUCED EQUATIONS
DISPERSION RELATION
TWO SCALES EIGENVALUE
GROWTH RATE (τ_{Hp}^{-1})
0.3
0.2
0.1
0
0
100
200
300
400
TOROIDAL MODE NUMBER

Fig. 5

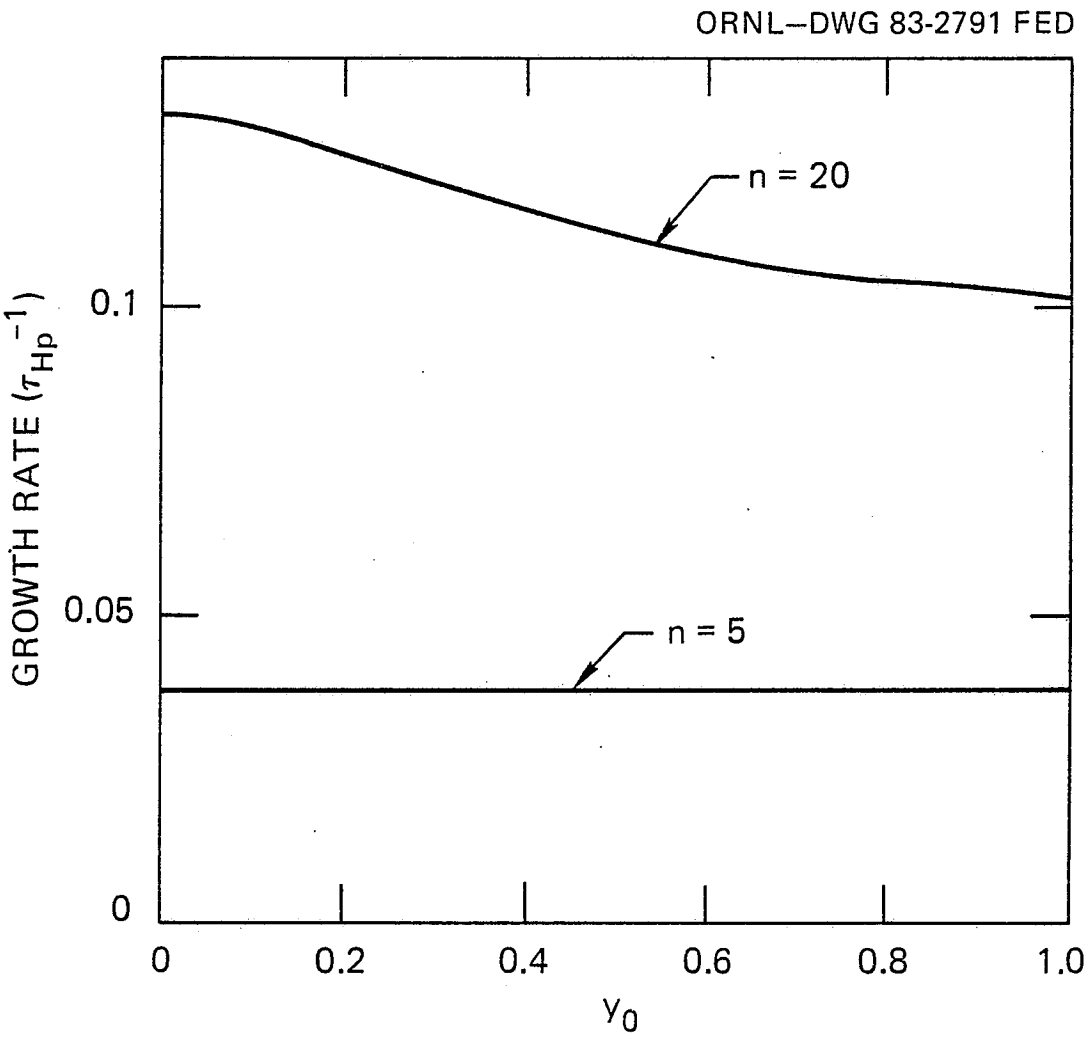
ORNL–DWG 83-2791 FED
n = 20
n = 5
0.1
0.05
0
GROWTH RATE (τ_{Hp}^{-1})
0
0.2
0.4
0.6
0.8
1.0
y_0

Fig. 6

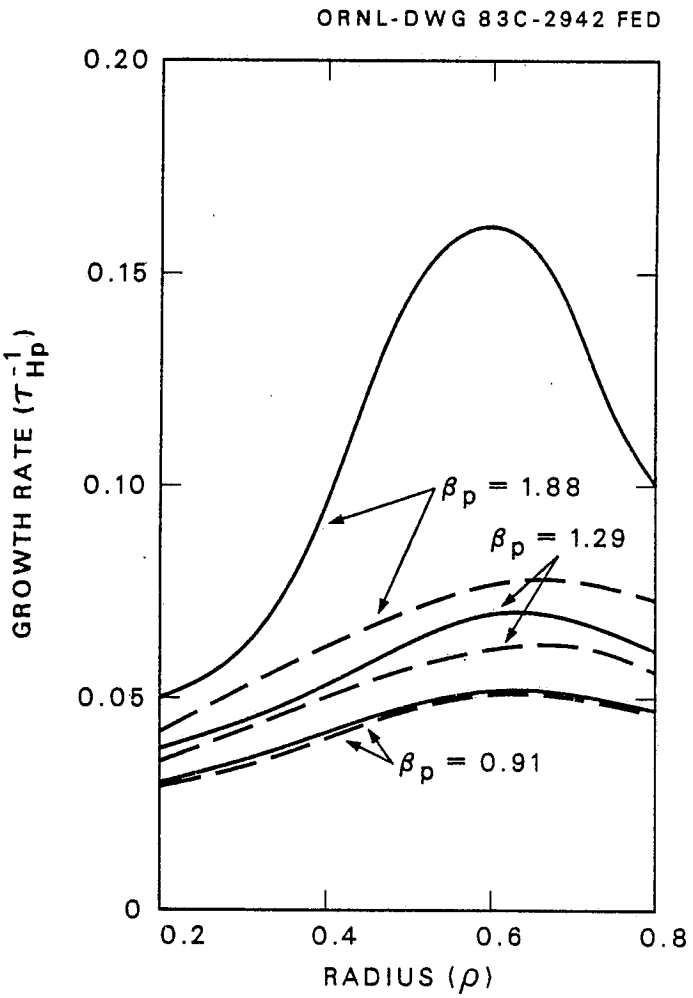
ORNL-DWG 83C-2942 FED
0.20
0.15
0.10
0.05
0
GROWTH RATE (τ_{Hp}^{-1})
β_p = 1.88
β_p = 1.29
β_p = 0.91
0.2
0.4
0.6
0.8
RADIUS (ρ)

Fig. 7

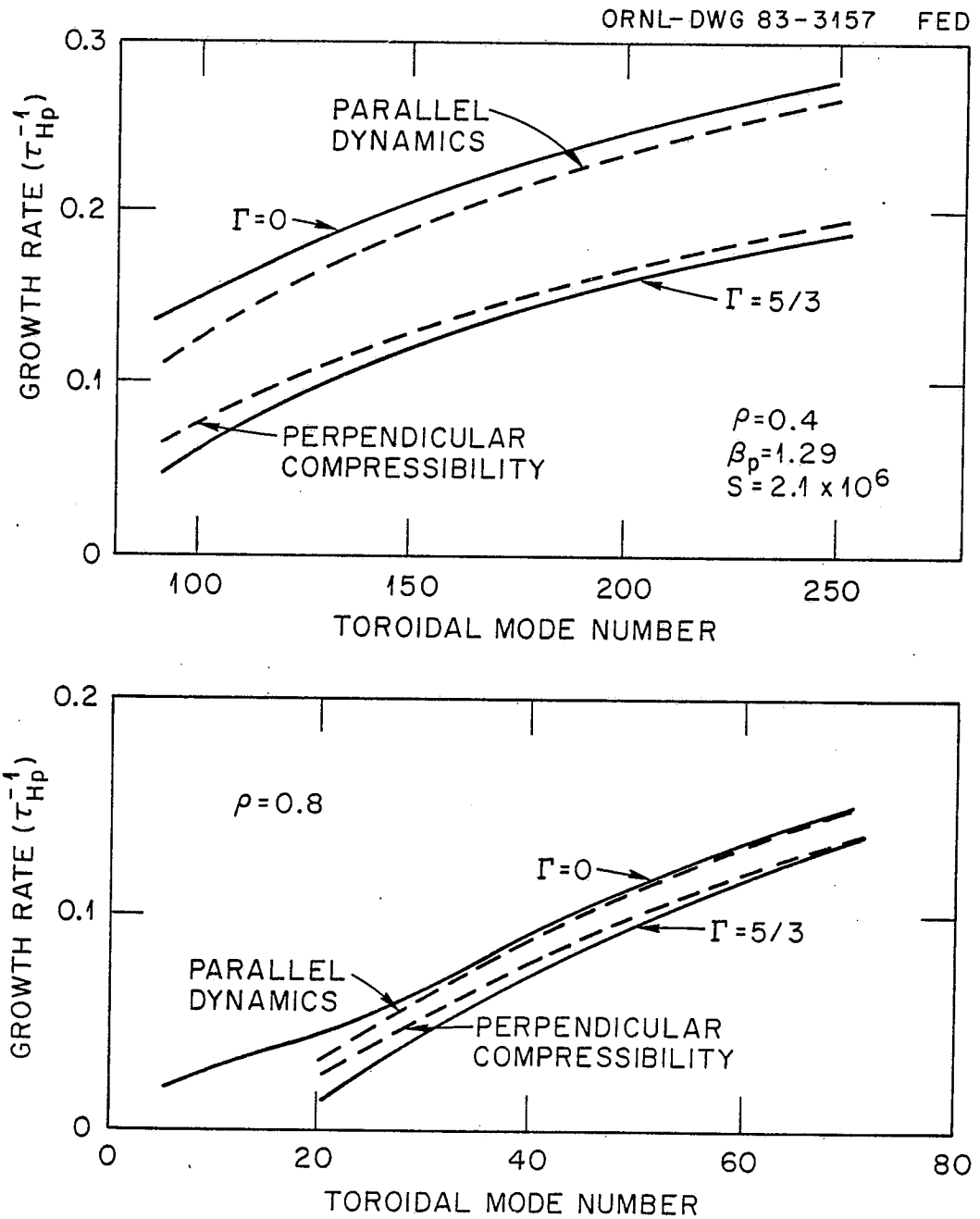
ORNL-DWG 83-3157 FED
GROWTH RATE (τ_{Hp}^{-1})
0.3
0.2
0.1
0
PARALLEL DYNAMICS
Γ=0
Γ=5/3
PERPENDICULAR COMPRESSIBILITY
ρ=0.4
β_p=1.29
S=2.1 x 10^6
100
150
200
250
TOROIDAL MODE NUMBER
GROWTH RATE (τ_{Hp}^{-1})
0.2
0.1
0
ρ=0.8
Γ=0
Γ=5/3
PARALLEL DYNAMICS
PERPENDICULAR COMPRESSIBILITY
0
20
40
60
80
TOROIDAL MODE NUMBER

Fig. 8

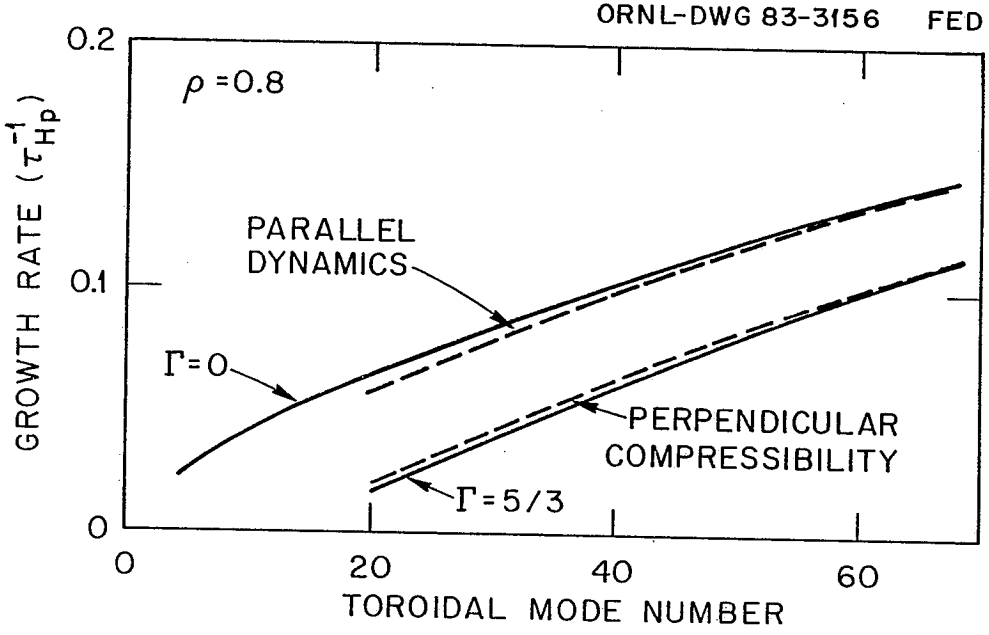
ORNL-DWG 83-3156 FED
0.2
0.1
0
ρ =0.8
GROWTH RATE (τ_{Hp}^{-1})
PARALLEL
DYNAMICS
Γ=0
PERPENDICULAR
COMPRESSIBILITY
Γ=5/3
0
20
40
60
TOROIDAL MODE NUMBER

Fig. 9

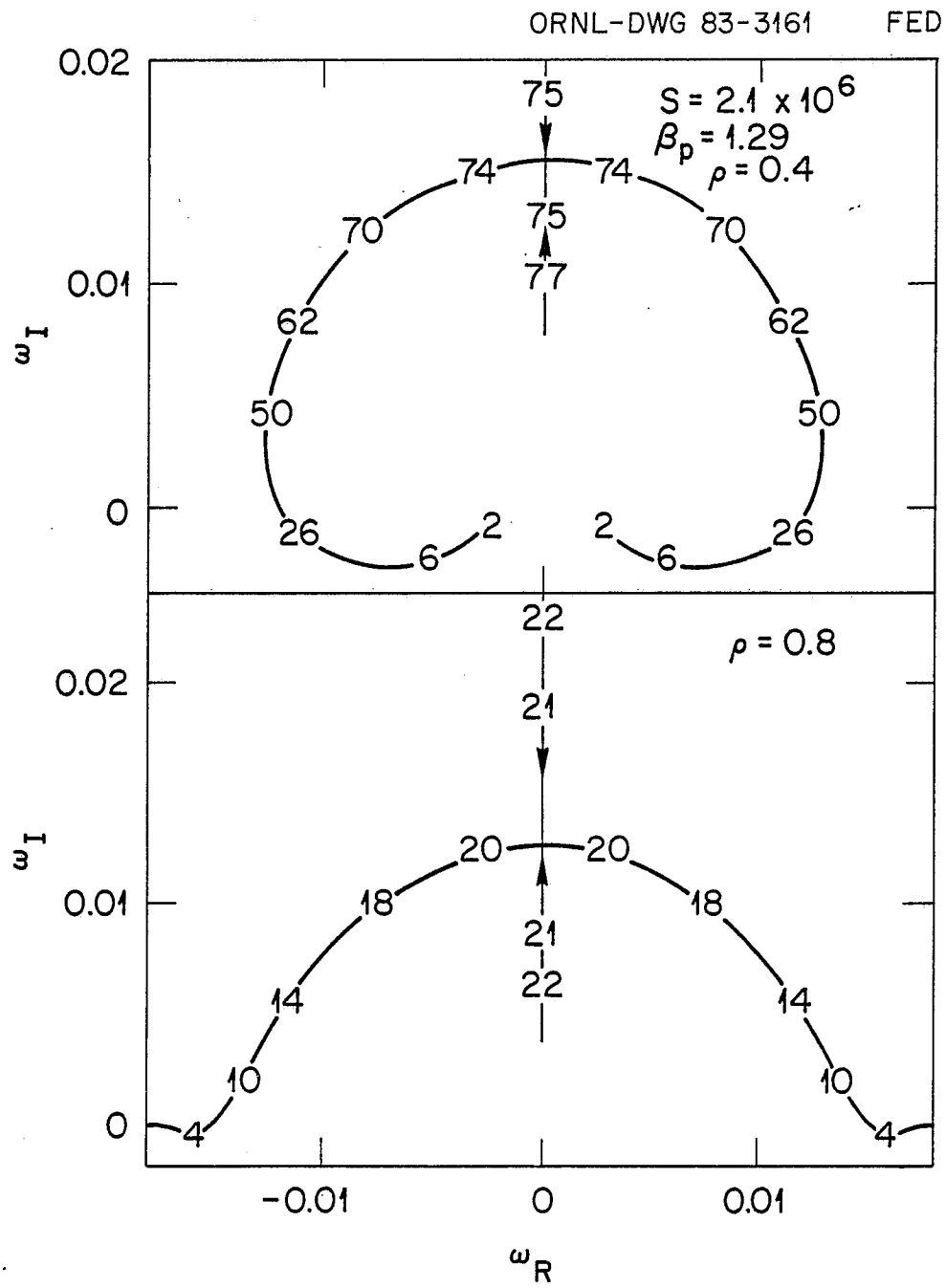
ORNL-DWG 83-3161 FED
S = 2.1 x 10^6
β_p = 1.29
ρ = 0.4
ρ = 0.8
ω_I
ω_R
0.02
0.01
0
-0.01
75
74
70
62
50
26
6
2
77
22
21
20
18
14
10
4

Fig. 10

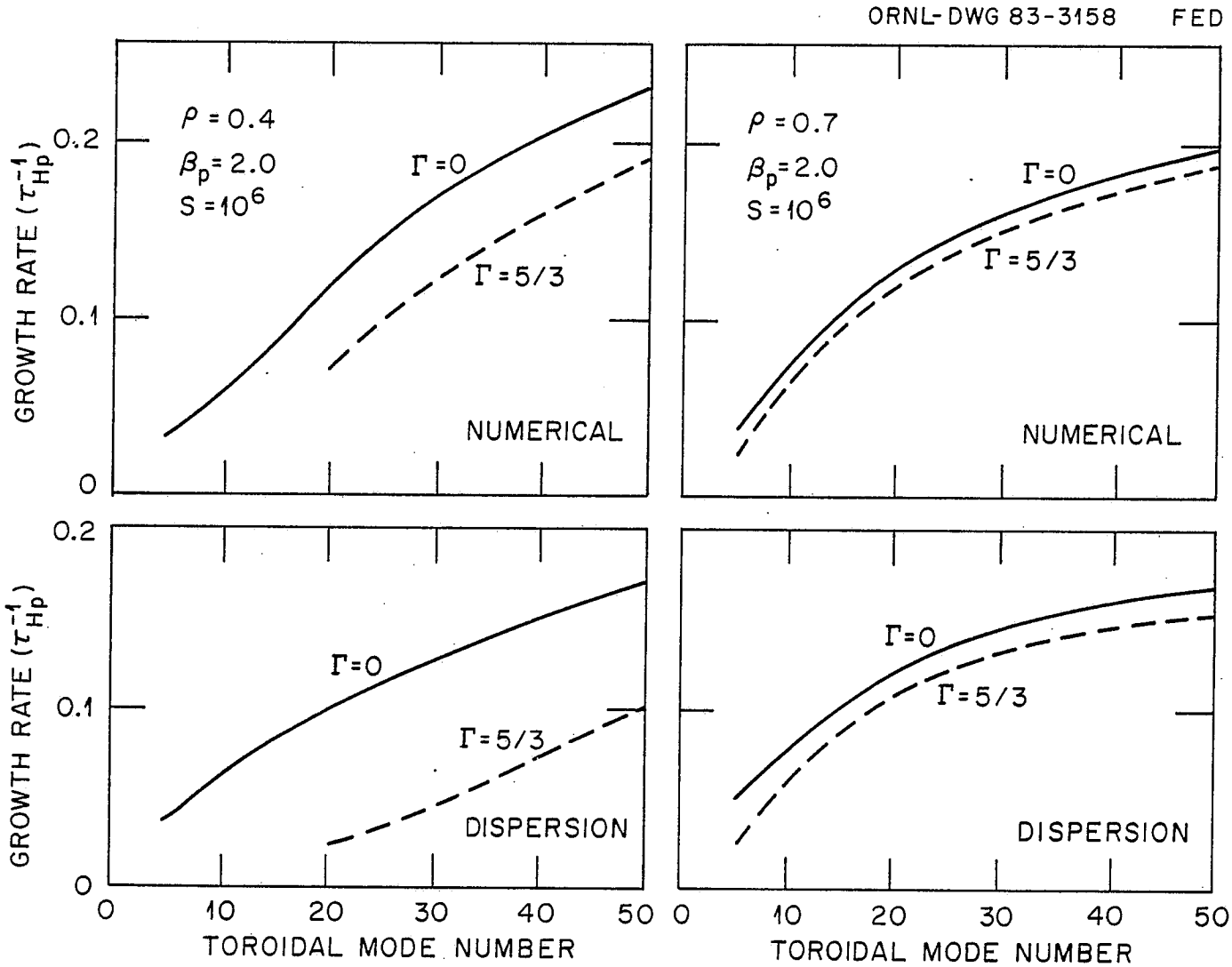
ORNL-DWG 83-3158 FED
ρ = 0.4
β_p = 2.0
S = 10^6
Γ = 0
Γ = 5/3
NUMERICAL
ρ = 0.7
β_p = 2.0
S = 10^6
Γ = 0
Γ = 5/3
NUMERICAL
GROWTH RATE (τ_Hp^-1)
0.2
0.1
0
Γ = 0
Γ = 5/3
DISPERSION
Γ = 0
Γ = 5/3
DISPERSION
0
10
20
30
40
50
TOROIDAL MODE NUMBER
TOROIDAL MODE NUMBER

Fig. 11

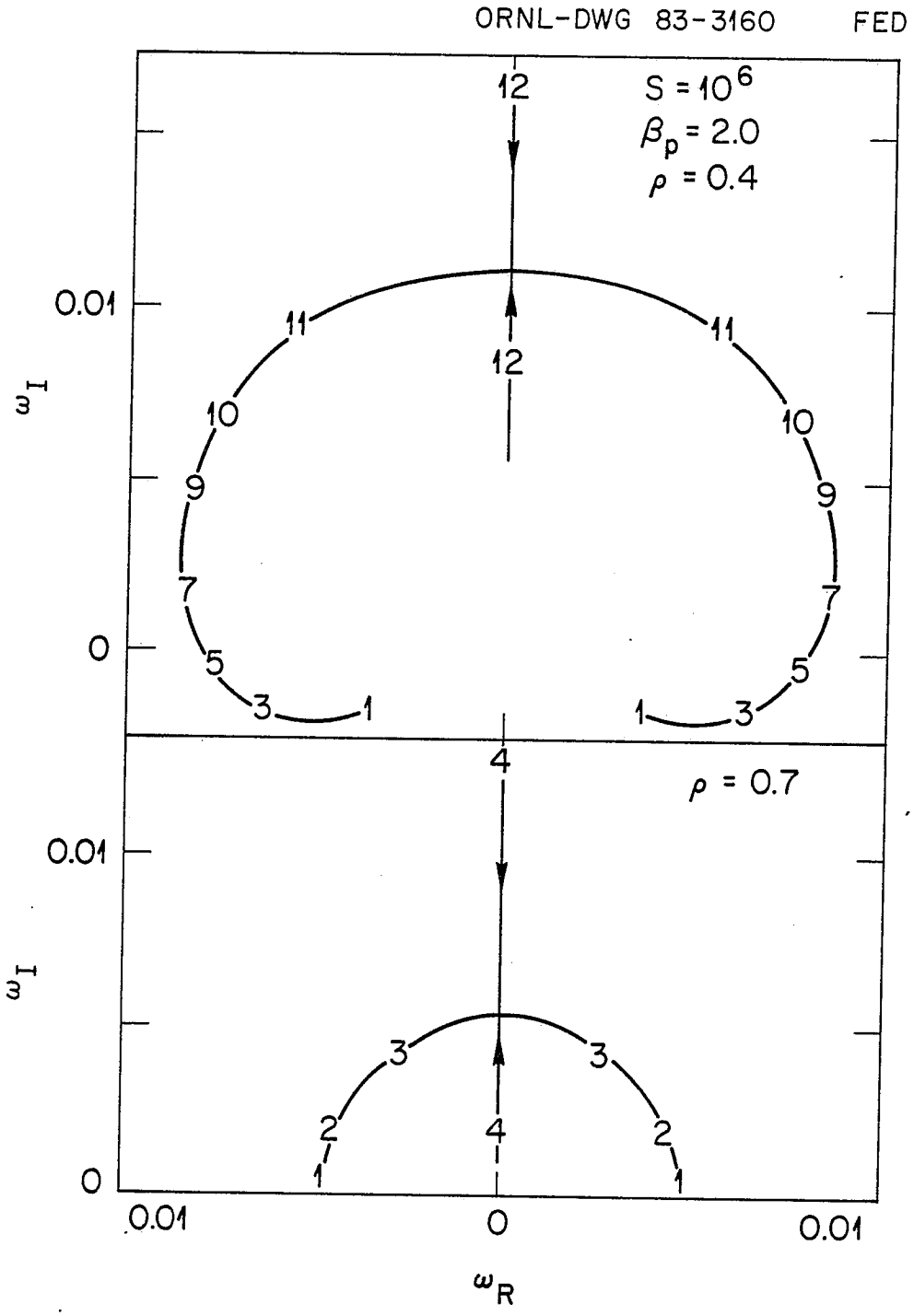

Fig. 12

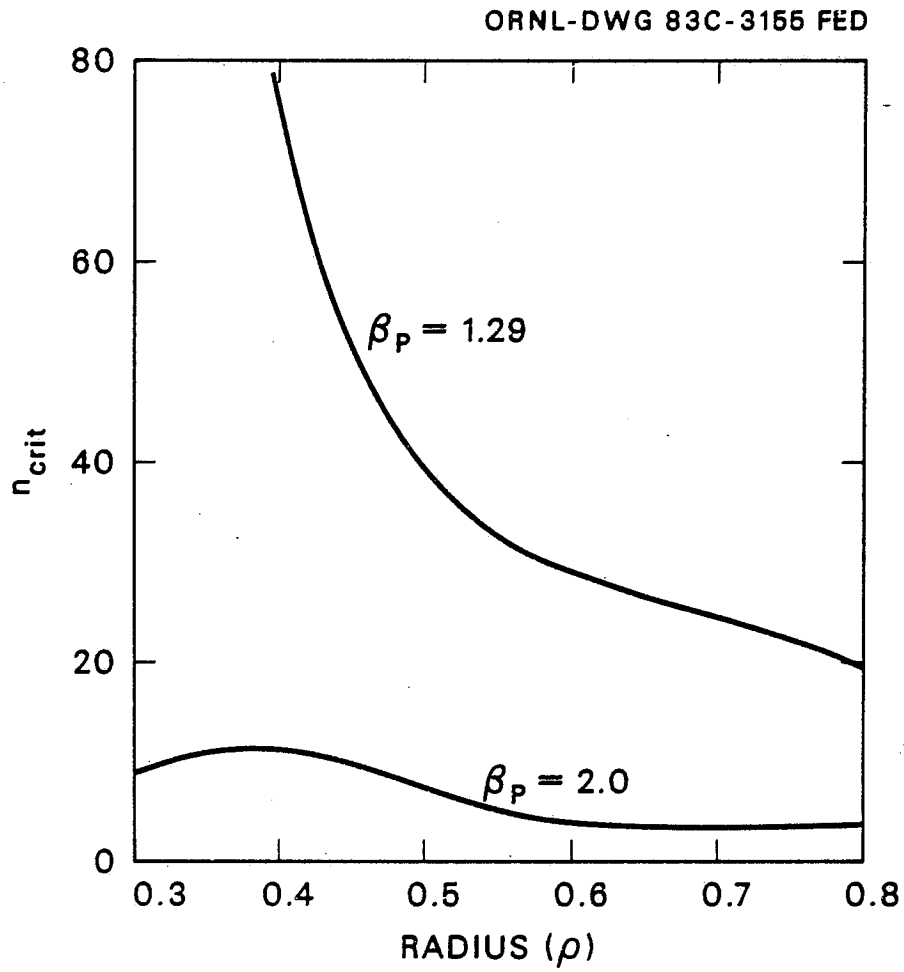
ORNL-DWG 83C-3155 FED
80
60
40
20
0
n_{crit}
$\beta_P = 1.29$
$\beta_P = 2.0$
0.3
0.4
0.5
0.6
0.7
0.8
RADIUS (ρ)

Fig. 13